Hypostatic jammed packings of frictionless nonspherical particles

Kyle VanderWerf,[1] Weiwei Jin,[2,3] Mark D. Shattuck,[4] and Corey S. O'Hern[1,3,5,6]

[1]*Department of Physics, Yale University, New Haven, Connecticut 06520, USA*

[2]*Department of Mechanics and Engineering Science, Peking University, Beijing 100871, China*

[3]*Department of Mechanical Engineering & Materials Science, Yale University, New Haven, Connecticut 06520, USA*

[4]*Benjamin Levich Institute and Physics Department, The City College of New York, New York, New York 10031, USA*

[5]*Department of Applied Physics, Yale University, New Haven, Connecticut 06520, USA*

[6]*Graduate Program in Computational Biology and Bioinformatics, Yale University, New Haven, Connecticut 06520, USA*

We perform computational studies of static packings of a variety of nonspherical particles including circulo-lines, circulo-polygons, ellipses, asymmetric dimers, dumbbells, and others to determine which shapes form packings with fewer contacts than degrees of freedom (hypostatic packings) and which have equal numbers of contacts and degrees of freedom (isostatic packings), and to understand why hypostatic packings of nonspherical particles can be mechanically stable despite having fewer contacts than that predicted from naive constraint counting. To generate highly accurate force- and torque-balanced packings of circulo-lines and cir-polygons, we developed an interparticle potential that gives continuous forces and torques as a function of the particle coordinates. We show that the packing fraction and coordination number at jamming onset obey a masterlike form for all of the nonspherical particle packings we studied when plotted versus the particle asphericity $\mathcal{A}$, which is proportional to the ratio of the squared perimeter to the area of the particle. Further, the eigenvalue spectra of the dynamical matrix for packings of different particle shapes collapse when plotted at the same $\mathcal{A}$. For hypostatic packings of nonspherical particles, we verify that the number of "quartic" modes along which the potential energy increases as the fourth power of the perturbation amplitude matches the number of missing contacts relative to the isostatic value. We show that the fourth derivatives of the total potential energy in the directions of the quartic modes remain nonzero as the pressure of the packings is decreased to zero. In addition, we calculate the principal curvatures of the inequality constraints for each contact in circulo-line packings and identify specific types of contacts with inequality constraints that possess convex curvature. These contacts can constrain multiple degrees of freedom and allow hypostatic packings of nonspherical particles to be mechanically stable.

I. INTRODUCTION

There have been a significant number of computational studies aimed at elucidating the jamming transition in static packings of frictionless spherical particles [1–3]. Key findings from these studies include (i) sphere packings at jamming onset at packing fraction ϕ_J are isostatic (where the number of contacts matches the number of degrees of freedom, as shown in Fig. 1), (ii) the coordination number, shear modulus, and other structural and mechanical quantities display power-law scaling as a function of the system's pressure P as packings are compressed above jamming onset at $P = 0$, and (iii) the density of vibrational modes develops a plateau at low frequencies ω that extends toward $\omega \to 0$ as the system approaches jamming onset. Many of these results are robust with respect to changes in the particle size polydispersity and different forms for the purely repulsive interparticle potential.

Most studies of jamming to date have been performed on packings of disks in two dimensions (2D) or spheres in three dimensions (3D). More recently, both computational and experimental studies have begun focusing on packings of nonspherical shapes, such as ellipsoids [4–11], sphero-cylinders [12–17], polyhedra [18,19], and composite particles [20–23]. In particular, there is a well-established set of results on packings of frictionless ellipses (or ellipsoids in 3D). In general, static packings of frictionless ellipses are *hypostatic* with fewer contacts than the number of degrees of freedom using naive contact counting. For amorphous mechanically stable (MS) packings of disks, the coordination number in the large-system limit is $z = 2d_f$ (where $d_f = 2$ is the number of degrees of freedom per particle) [24]. Thus, one might expect that the coordination number for ellipses in 2D would jump from $z = 4$ to 6 (with $d_f = 3$) for any aspect ratio $\alpha > 1$. However, $z(\alpha)$ increases continuously from 4 at $\alpha = 1$ and remains less than 6 for all α. We have shown that the number of missing contacts exactly matches the number of "quartic" eigenmodes from the dynamical matrix for which the potential energy increases as the fourth power of the displacement for perturbations along the corresponding eigenmode [6]. In addition, the packing fraction at jamming onset $\phi_J(\alpha)$ possesses a peak near $\alpha \approx 1.5$, and then decreases for increasing α.

Are these results for ellipses similar to those for all other nonspherical or elongated particle shapes? Prior results for packings of sphero-cylinders have shown that they are hypostatic [16]. However, packings of composite particles formed from collections of disks (2D) [20,25] or spheres (3D) [21] are isostatic at jamming onset. Unfortunately, very few studies explicitly check whether hypostatic packings are mechanically
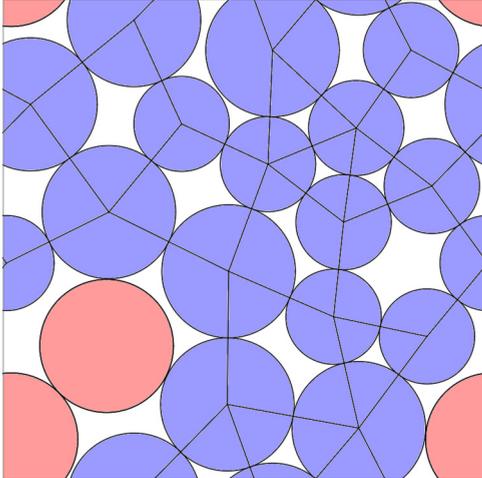
FIG. 1. An isostatic packing of $N = 18$ bidisperse disks (9 large and 9 small with diameter ratio $r = 1.4$) in a square box with periodic boundary conditions at jamming onset $\phi_J = 0.835$. Blue disks form the force-bearing backbone, and red disks are "rattler" disks that possess fewer than three contacts. This isostatic packing possesses $N_c = N_c^0 = 2(N - N_r) - 1 = 31$ contacts (indicated by black solid lines), where N_c^0 is the isostatic number of contacts.

TABLE I. A list of the nine strictly or effectively convex, non-spherical particle shapes studied in this article, along with the ranges of aspect ratio α and asphericity $\mathcal{A}$ that we considered.

Particle shape	$\alpha - 1$	$\mathcal{A} - 1$
Circulo-line	10^{-3}–4	4.05×10^{-7}–1.06
Circulo-triangle		$10^{-6.5}$–0.4
Circulo-pentagon		$10^{-6.5}$–0.4
Circulo-octagon		$10^{-6.5}$–0.4
Circulo-decagon		$10^{-6.5}$–0.1
Dimer	0.571	0.349
Dumbbell	2–4	0.514–2.405
Reuleaux triangle		0.114
Ellipse	10^{-4}–0.9	3.75×10^{-9}–0.161

stable. The goal of this article is to determine which particle shapes can form mechanically stable (i.e., jammed), hypostatic packings, identify a key shape parameter that controls the forms of the coordination number z and packing fraction ϕ_J, and gain a fundamental understanding for why hypostatic packings are mechanically stable, even at jamming onset $P = 0$.

To address these questions, we generate static packings using a compression and decompression scheme coupled with energy minimization for nine different particle shapes (ellipses, circulo-lines, circulo-triangles, circulo-pentagons, circulo-octagons, circulo-decagons [26], dimers [20], dumbbells [27], and Reuleaux triangles [28]) in 2D. These particle shapes can all be classified as strictly convex or "effectively convex," meaning that the accessible contact surface for each particle is nowhere locally concave. In this paper, we restrict our studies to strictly convex or effectively convex particle shapes. To study such a wide range of particle shapes, we developed a fully continuous and differentiable interparticle potential for circulo-lines and circulo-polygons, which allows us to generate packings with extremely accurate force and torque balance at very low pressure [29–33]. We find several important results. First, we show that the jammed packing fraction for the particle shapes that yield hypostatic packings collapses onto a masterlike curve when plotted versus the asphericity parameter $\mathcal{A} = p^2/4\pi a$, where p is the perimeter and a is the area of the particle. We also show that the coordination number $z(\mathcal{A})$ follows a masterlike curve when contacts between nearly parallel circulo-lines or nearly parallel sides of circulo-polygons are treated properly. In addition, for packings of circulo-lines, we calculate the fourth derivatives of the total potential energy along the quartic modes of the dynamical matrix [6] and show that the fourth derivatives are nonzero as $P \to 0$, which proves that these hypostatic packings are mechanically stable. Finally, we calculate the principal curvatures of the constraint surfaces in configuration space

defined by each contact to identify which types of contacts in packings of circulo-lines allow them to be mechanically stable, while hypostatic.

This article is organized as follows. In Sec. II, we describe the compression and decompression plus minimization method we use to generate static packings of convex or effectively convex, nonspherical particles. In Sec. III A, we present examples of static packings of several different strictly and effectively convex, nonspherical particle shapes to put forward a conjecture concerning which nonspherical particle shapes form hypostatic packings and which always form isostatic packings. In Sec. III B, we show that the packing fraction $\phi(\mathcal{A})$ and coordination number $z(\mathcal{A})$ at jamming onset display masterlike forms when plotted versus the particle asphericity $\mathcal{A}$, for the nonspherical particle shapes that yield hypostatic packings. In this section, we also show results for the calculations of the fourth derivatives of the total potential of the static packings in the directions of dynamical matrix eigenmodes. Finally, in Sec. III C, we calculate and analyze the principal curvatures of the constraint surfaces given by the interparticle contacts to understand the grain-scale mechanisms that enable hypostatic packings to be mechanically stable. We also include three appendices. Appendix A describes the development of a continuous and differentiable interparticle repulsive potential between circulo-lines and circulo-polygons, which allows us to generate extremely accurate force- and torque-balanced jammed packings near zero pressure. Appendix B describes how we generate different circulo-polygon shapes at constant asphericity $\mathcal{A}$. Finally, in Appendix C, we provide expressions for the elements of the dynamical matrix for packings of circulo-polygons.

II. METHODS

Using computer simulations, we generate static packings of frictionless, nonspherical, convex or effectively convex particles in 2D. The particles are nearly hard in the sense that we consider mechanically stable packings in the zero-pressure limit. We study nine different particle shapes: circulo-lines, circulo-triangles, circulo-pentagons, circulo-octagons, circulo-decagons, Reuleaux triangles, ellipses, dumbbells, and dimers. (See Table I.) We focus on bidisperse mixtures in which half of the particles are large and half are small to prevent crystallization [1,34]. The large particles have areas that satisfy

$a_L = 1.4^2 a_S$, where $a_{L,S}$ are the areas of the large and small particles, respectively. Both particles have the same mass m. We generated static packings at fixed asphericity $\mathcal{A}$ for the large and small particles over a wide range of $\mathcal{A}$. We employ periodic boundary conditions in square domains with edge length $L = 1$ and system sizes that vary from $N = 24$ to 480 particles. Note that the term "effectively convex particle shapes" stands for "shapes whose accessible contact surface is nowhere locally concave." Our studies include dimers (which possess two points on the surface that are concave), circulo-lines (which contain regions of zero curvature), ellipses, and other explicitly convex particles.

We assume that particles i and j interact via the purely repulsive, pairwise linear spring potential,

$$U(r_{ij}) = \frac{k}{2}(\sigma_{ij} - r_{ij})^2 \Theta(\sigma_{ij} - r_{ij}), \qquad (1)$$

where k is the spring constant of the interaction and $\Theta(x)$ is the Heaviside step function. Below, lengths, energies, and pressures will be expressed in units of L, kL^2, and k, respectively. For disks, r_{ij} is the separation between the centers of disks i and j, and $\sigma_{ij} = R_i + R_j$ is the sum of the radii of disks i and j.

For dimers, i.e., composite particles formed from two circular monomers, r_{ij} is the center-to-center separation between each pair of interacting monomers, and σ_{ij} is the sum of the radii of those monomers. A Reuleaux triangle is a shape that is constructed by joining three circular arcs of equal radius such that their intersection points (vertices of the Reuleaux triangle) are the centers of each circle. For this shape, we first identify whether two arcs are overlapping or whether a vertex is overlapping an arc. We then set r_{ij} in Eq. (1) to be the distance between the center points of the overlapping arcs (in the case of two overlapping arcs) or the distance between the center point of the arc and the vertex (in the case of a vertex overlapping an arc). We set σ_{ij} to be the sum of the radii of the two overlapping arcs, or the radius of the single arc when a vertex is overlapping an arc. (See Fig. 2.)

For ellipses, we take r_{ij} to be the distance between the centers of the particles, and σ_{ij} to be the center-center distance that would bring the particles exactly into contact at their current orientations [6]. For dumbbell-shaped particles, we have multiple possible cases for r_{ij}, depending on their orientations. We calculate r_{ij} either as the distance between each pair of circular ends, or between each circular end and
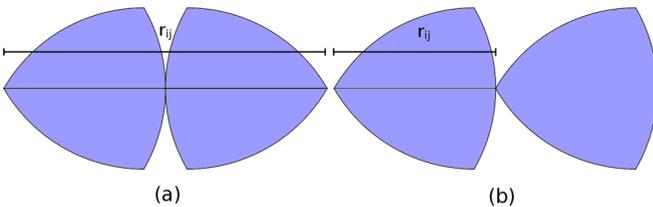

FIG. 2. Definition of the separation r_{ij} between two Reuleaux triangles when (a) the two circular arcs are overlapping and (b) a vertex is overlapping one of the circular arcs. In case (a), r_{ij} is the distance between the vertices at the centers of the corresponding arcs. In case (b), r_{ij} is the distance between the arc's central vertex and the vertex overlapping the arc.

the other particle's shaft, with σ_{ij} chosen to be the sum of the relevant radii in each case. The repulsive contact interactions between circulo-lines and circulo-polygons are calculated in a similar fashion to dumbbells. However, because the regions of changing curvature in the case of circulo-lines and circulo-polygons are accessible, unlike in the dumbbell case, additional constraints in the potential are necessary to prevent discontinuities in the pairwise torques and forces. For a thorough explanation of how we define a continuous and differentiable repulsive linear spring potential between circulo-lines and circulo-polygons, see Appendix A).

In this article, our method for generating jammed packings of nonspherical particles employs conjugate gradient energy minimization, which we have used extensively for studying disordered, jammed disk packings [35]. These methods are similar to "rapid" energy minimization to zero temperature, which can be achieved using steepest descent, where particle forces are proportional to velocities. More generally, we can use molecular dynamics (MD) simulation methods to generate jammed packings of spherical and nonspherical particles. With MD, we can employ a range of damping parameters, even small values, where the energy is drained from the system slowly. However, we use conjugate gradient (CG) energy minimization in the present studies since CG is analogous to a "fast" thermal quench and yields exclusively disordered packings.

To generate static packings, we successively compress and decompress the system with each compression or decompression step followed by the conjugate gradient method to minimize the total potential energy $U = \sum_{i>j} U(r_{ij})$. We use a binary search algorithm to push the system to a target pressure $P = P_0$. If $P > P_0$, the system is decompressed isotropically, and if $P < P_0$, the system is compressed isotropically. Subsequently, we perform minimization of the enthalpy [36] $H = U + P_0 A$, where A is the area of the system, the pressure $P = -dU/dA$, and $P_0 = 10^{-9}$ is the target pressure, with the particle positions and the box edge length as the degrees of freedom. Using this algorithm, we achieve accurate force and torque balance such that the squared forces f_i^2 and torques τ_i^2 on a given particle i do not exceed 10^{-25}.

After generating each static packing, we calculate its dynamical matrix M, which is the Hessian matrix of second derivatives of the total potential energy U with respect to the particle coordinates:

$$M_{ij} = \frac{\partial^2 U}{\partial \xi_i \partial \xi_j}, \qquad (2)$$

where $\xi_i = x_i$, y_i, and θ_i, x_i and y_i are the coordinates of the geometric center of particle i, and θ_i characterizes the rotation angle of particle i. We then calculate the $3N$ eigenvalues λ_i of M, and the corresponding eigenvectors $\vec{\lambda}_i$ with $\vec{\lambda}_i^2 = 1$. For more details on the calculation of the dynamical matrix elements, see Appendix C.

III. RESULTS

Our results are organized into three subsections. In Sec. III A, we discuss which nonspherical particle shapes give rise to hypostatic packings, and then propose specific criteria that nonspherical particle shapes must satisfy to yield hypostatic packings. In Sec. III B, we show the variation of

the packing fraction ϕ and coordination number z at jamming onset with particle asphericity $\mathcal{A}$ for packings of circulo-lines, circulo-polygons, and ellipses. Finally, in Sec. III C, we calculate the principal curvatures of the inequality constraints in configuration space arising from interparticle contacts for hypostatic packings of circulo-lines to identify the specific types of contacts that allow static packings to be hypostatic, yet mechanically stable.

A. Nonspherical particle shapes that give rise to hypostatic packings

In this section, we discuss results for the contact number of static packings containing a variety of nonspherical particle shapes. Based on these results, we propose that strictly and effectively convex frictionless particles will form hypostatic packings if both of the following two criteria are satisfied: (i) the particle has one or more nontrivial rotational degrees of freedom, and (ii) the accessible (nonexcluded) contact area cannot be achieved by a union of a finite number of disks. Below, we show several examples of systems that satisfy and do not satisfy these criteria.

First, disks do not satisfy (i) or (ii), and hence our conjecture predicts that disks will form isostatic, not hypostatic, packings. Next, we consider packings of circulo-lines that are prevented from rotating, and thus the particle's orientation remains the same over the course of the packing simulations. [See Fig. 3(a).] These particles obey criterion (ii), as a circulo-line can only be achieved by a union of an *infinite* number of disks, but fail to meet criterion (i). Hence, the above conjecture predicts that these particles will form isostatic, not hypostatic, packings. We also generated packings of bidisperse asymmetric dimers [Fig. 3(b)]. These particles meet criterion (i) since we allow them to rotate, but fail to meet criterion (ii) since dimers are made up of a union of two disks. Thus, our conjecture predicts that these particles will form isostatic, not hypostatic, packings, as shown in Fig. 3(b).

Finally, we generated packings of rotating circulo-lines, as well as Reuleaux triangles, examples of which are pictured in Figs. 3(c) and 3(d), respectively. Both particles meet criterion (i) since they are allowed to rotate. Circulo-lines meet criterion (ii) as stated earlier. Reuleaux triangles also meet criterion (ii). Despite being comprised of a finite number of circular arcs, it is impossible to represent them as a finite number of complete disks. Therefore, since both particle shapes meet both criteria, our conjecture predicts that they will form hypostatic, not isostatic, packings. Ellipses also meet criteria (i) and (ii) and form hypostatic packings [6].

The importance of specifying "accessible (nonexcluded) contact area" in criterion (ii) can be demonstrated by the two packings of dumbbells in Fig. 4. In both cases, the particles are allowed to rotate, so criterion (i) is satisfied. The packing in Fig. 4(a) also satisfies criterion (ii) because the shaft is part of the accessible contact surface of the constituent particles, and the shaft cannot be expressed as a finite union of disks. Thus, we expect hypostatic packings for the dumbbells in Fig. 4(a). In contrast, in Fig. 4(b), the shaft is not part of the accessible contact surface because it is too short to allow the end disks of other particles to come into contact with it. Thus, the particles in Fig. 4(b) do not satisfy criterion (ii) because the accessible
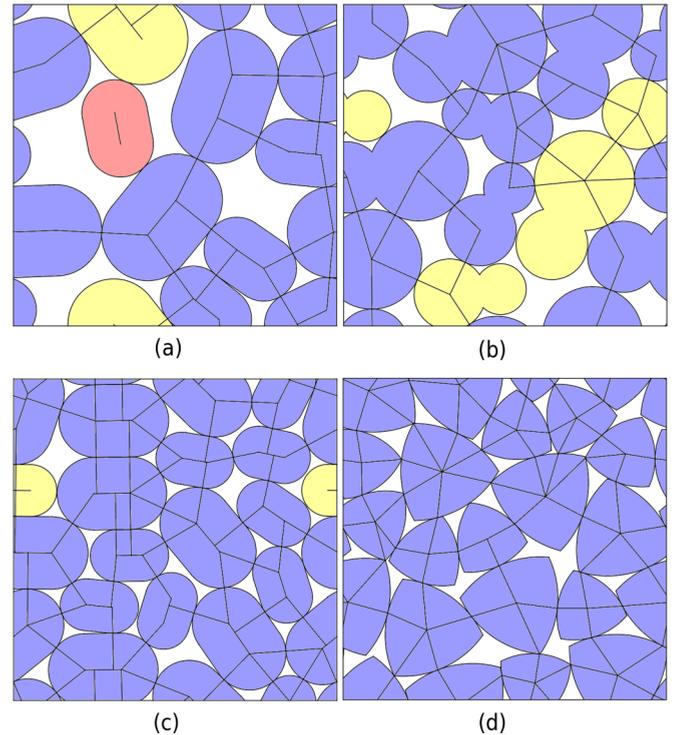

FIG. 3. Two isostatic [(a) and (b)] and two hypostatic packings [(c) and (d)] of nonspherical particles. (a) This packing with $\phi = 0.782$ consists of 10 nonrotating circulo-lines with asphericity $\mathcal{A} = 1.06$. The red particle is a rattler with two unconstrained degrees of freedom, and the yellow particle is a slider with one unconstrained degree of freedom. The blue and yellow particles form an isostatic contact network with $N_c = 2N - 4 = 16$ contacts, where we have subtracted off three additional contacts due to the rattler and slider particles. (b) This packing with $\phi = 0.828$ consists of 10 asymmetric dimers. The two monomers on a given dimer have a diameter ratio $r = 1.4$ and the ratio of the lengths of large and small dimer axes is $d = 1.4$. The three yellow "rotator" particles each have one unconstrained rotational degree of freedom. The particles form an isostatic contact network with $N_c = 3N - 4 = 26$ contacts, where we have subtracted off three additional contacts due to the rotator particles. (c) This packing with $\phi = 0.892$ consists of 18 rotating circulo-lines with asphericity $\mathcal{A} = 1.06$. The yellow particle is a slider with one unconstrained degree of freedom. If the particles formed an isostatic contact network, it would possess $N_c = 3N - 2 = 52$ contacts. However, we find $N_c = 46$. (d) This packing with $\phi = 0.874$ consists of 18 Reuleaux triangles. If the system were isostatic, $N_c = 3N - 1 = 53$, however, we find $N_c = 43$.

contact surface can be achieved by a union of two disks. We expect packings generated using the dumbbells in Fig. 4(b) to be isostatic.

B. Packing fraction, coordination number, and eigenvalues of the dynamical matrix

In this section, we describe studies of the packing fraction and coordination number of packings of nonspherical particles at jamming onset as a function of the particle asphericity $\mathcal{A}$. Note that for each particle type, other than Reuleaux triangles, studied in this section (namely, circulo-lines, ellipses, circulo-triangles, circulo-pentagons, circulo-octagons,
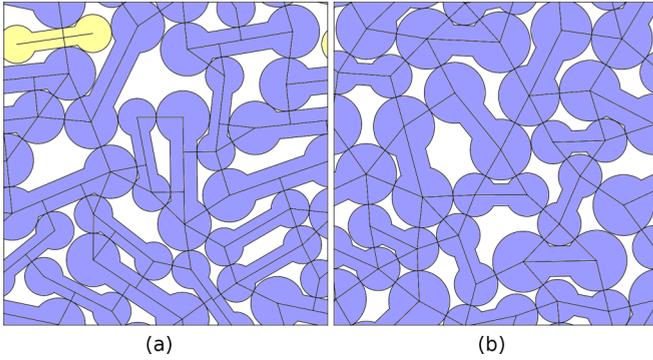
FIG. 4. (a) A hypostatic and (b) an isostatic packing of 18 dumbbells, with packing fractions $\phi = 0.769$ and 0.806, respectively. In (a) and (b), the shaft half-width is equal to half of the radius of the end disks. In (a) the length of the shaft is 4 times the disk radius, whereas in (b), the shaft length is 2.4 times the disk radius. In (a), the yellow particle has one unconstrained degree of freedom. Thus, if the particles formed an isostatic contact network, $N_c = 3N - 2 = 52$. The packing is hypostatic with $N_c = 51$. In (b), the packing has no particles with unconstrained degrees of freedom. This packing is isostatic with $N_c = 3N - 1 = 53$.

and circulo-decagons), we are considering a *family* of shapes of that type, whose asphericity can be varied continuously. We also calculate the eigenvalues of the dynamical matrix for packings of circulo-lines and circulo-polygons and show the eigenvalue spectrum as a function of decreasing pressure. We find that hypostatic packings possess a band of eigenvalues, i.e., the "quartic modes," for which the energy increases as the fourth power in amplitude when we perturb the system along their eigendirections. These quartic modes are not observed in isostatic packings. We further show that the fourth derivative of the total potential energy in the direction of these quartic modes does not vanish at zero pressure, proving that packings possessing quartic modes are mechanically stable, despite being hypostatic.

In Fig. 5, we plot the average packing fraction at jamming onset versus $\mathcal{A}$ for all of the nonspherical particles we considered. The data for $\langle \phi \rangle$ nearly collapse onto a master curve, which tends to $\langle \phi \rangle \approx 0.84$ for small $\mathcal{A} - 1$, as found for packings of bidisperse disks [35], forms a peak near $\mathcal{A} - 1 \approx 10^{-1}$, and decreases strongly for $\mathcal{A} - 1 > 10^{-1}$. This result suggests that the asphericity can serve as common descriptor of the structural and mechanical properties of packings of nonspherical particles, i.e., jammed packings with similar $\mathcal{A}$ will possess similar properties.

In Fig. 6, we plot the average coordination number

$$\langle z \rangle = \frac{2(N_c + 1)}{N - N_r - N_s/3}, \tag{3}$$

where N_c is the number of contacts in the packing. The $+1$ in the factor of $N_c + 1$ is included to account for the -1 in the expression for the number of contacts $N_c = N_c^0 = 3N - 1$ in isostatic packings of nonspherical particles in 2D, where N_c^0 is the isostatic number of contacts. N_r is the number of rattler particles that have unconstrained translational and rotational degrees of freedom. N_s is the number of "slider" particles with a single unconstrained translational degree of freedom.
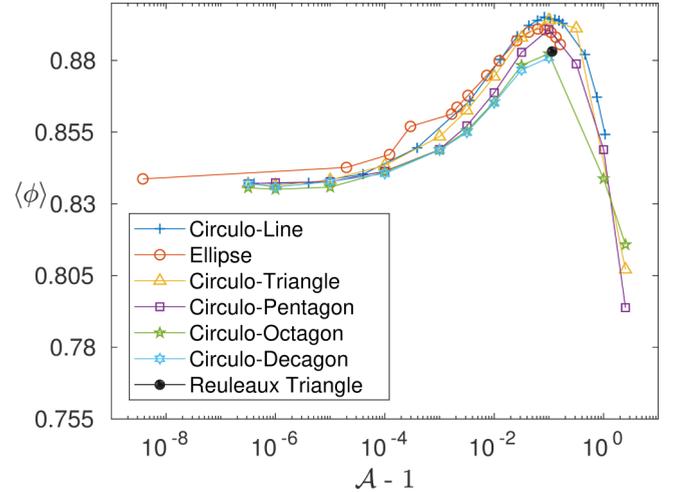

FIG. 5. Packing fraction at jamming onset $\langle \phi \rangle$ (averaged over 50 packings with random initial conditions) plotted versus asphericity $\mathcal{A} - 1$ for a variety of nonspherical shapes: ellipses (circles), circulo-lines (plus signs), circulo-triangles (triangles), circulo-pentagons (squares), circulo-octagons (five-pointed stars), circulo-decagons (six-pointed stars), and Reuleaux triangles (filled black circle). The packings include $N = 100$ particles, except for the ellipse packings, which contain $N = 480$ particles.

An example of a slider particle is the yellow particle in the packing of circulo-lines in Fig. 3(c), which can translate along its long axis without energy cost. Defining the coordination number as in Eq. (3) ensures that an isostatic packing of circulo-lines, circulo-polygons, or other nonspherical particles will have $\langle z \rangle = 6$. If $\langle z \rangle < 6$, the packing is hypostatic.

In Fig. 6, we show the coordination number $\langle z \rangle$ in Eq. 3 versus $\mathcal{A} - 1$ for packings of ellipses and circulo-lines for two ways of defining a contact between two nearly parallel circulo-lines. At low asphericities, where the particle shape approaches a disk, a nearly parallel contact is only able to
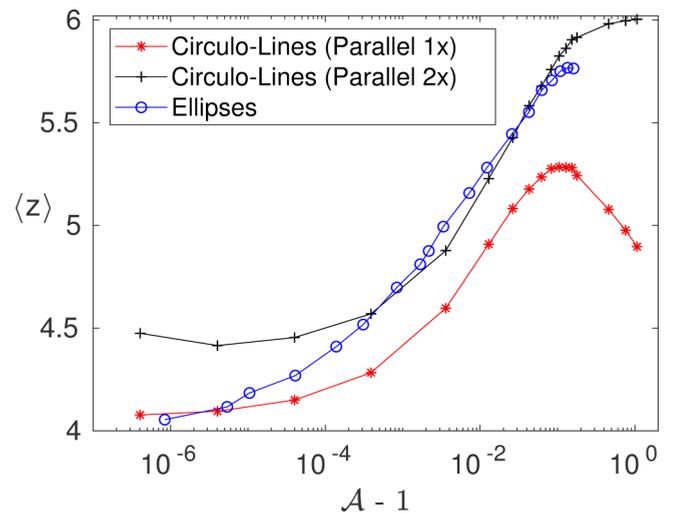

FIG. 6. Coordination number $\langle z \rangle$ [defined in Eq. (3)] at jamming onset as a function of asphericity $\mathcal{A} - 1$ for ellipses (circles) and circulo-lines, counting a contact between nearly parallel circulo-lines as one contact (asterisks) or two contacts (plus signs).

apply a small torque to the two contacting particles, making it unlikely to constrain a rotational degree of freedom in addition to a translational degree of freedom. Thus, at low asphericities, nearly parallel contacts should only be counted as a single constraint. In Fig. 6, we show that $\langle z \rangle$ for ellipses and circulo-lines (counting nearly parallel contacts once) both approach 4 in the limit $\mathcal{A} - 1$ tends to zero.

In contrast, at large asphericities, nearly parallel contacts between two circulo-lines prevent the particles from rotating and translating (in a direction perpendicular to their shafts). Thus, for large $\mathcal{A} - 1$, nearly parallel contacts should be counted as two constraints. In Fig. 6, we show that the coordination number $\langle z \rangle$ for packings of circulo-lines approaches 6 in the large $\mathcal{A} - 1$ limit when nearly parallel contacts are counted twice. These results suggest that we must interpolate between counting parallel contacts once at low asphericities, and counting them twice as the asphericity increases.

One way to resolve the question of whether to count a nearly parallel contact between nonspherical particles as one or two constraints is to calculate the dynamical matrix (all second derivatives of the total potential energy with respect to the particle coordinates) of the static packings, and examine the spectrum of the dynamical matrix eigenvalues, which in the harmonic approximation give the vibrational frequencies of the packing [37]. For details on the calculation of the entries of the dynamical matrix for circulo-lines and circulo-polygons, see Appendix C.

In Fig. 7, we show the eigenvalue spectrum (sorted from smallest to largest) for static packings of circulo-lines over a wide range of aspect ratios $\mathcal{A} - 1$ from $\approx 10^{-6}$ to 1 (decreasing from top to bottom). As found in Ref. [5] for ellipse packings, the eigenvalue spectra for packings of circulo-lines possess several distinct regions. Region 0 ($\lambda_i \lesssim 10^{-14}$, which is set by numerical precision) corresponds to unconstrained degrees of freedom, such as overall translations from periodic boundary conditions, and rattler and slider particles. Region 1 ($10^{-14} \lesssim \lambda_i \lesssim 4 \times 10^{-8}$) corresponds to "quartic modes," whose number is determined by the number of missing contacts relative to the isostatic contact number. For the asphericities we consider, regions 2 and 3 correspond to eigenmodes with predominantly rotational and translational motion, respectively.

If we focus on all but the three smallest asphericities (i.e., the three rightmost curves in Fig. 7), we can define a cutoff value λ_c that clearly separates regions 1 and 2. For packings of $N = 100$ circulo-lines at pressure $P_0 = 10^{-9}$, $\lambda_c \approx 4 \times 10^{-8}$. For asphericities where λ_c distinguishes regions 1 and 2, the number of contacts in packings of circulo-lines satisfies $N_c = N_c^0 - N_1$, where N_1 is the number of eigenvalues in region 1. A key observation is that defining the number of contacts in this way for intermediate and high asphericities is the same as if N_c is determined by the number of particle contacts, with nearly parallel contacts counted twice. For asphericities where the difference between regions 1 and 2 is more ambiguous, we still use λ_c to determine whether a given eigenvalue belongs to region 1 or 2. For the lowest asphericities, we find that defining $N_c = N_c^0 - N_1$ corresponds to counting one constraint for each nearly parallel contact.

In Fig. 8, we plot the average coordination number $\langle z \rangle$ from Eq. (3) using $N_c = N_c^0 - N_1$ versus $\mathcal{A} - 1$ for $N = 100$ packings of circulo-lines and circulo-polygons. At low asphericities
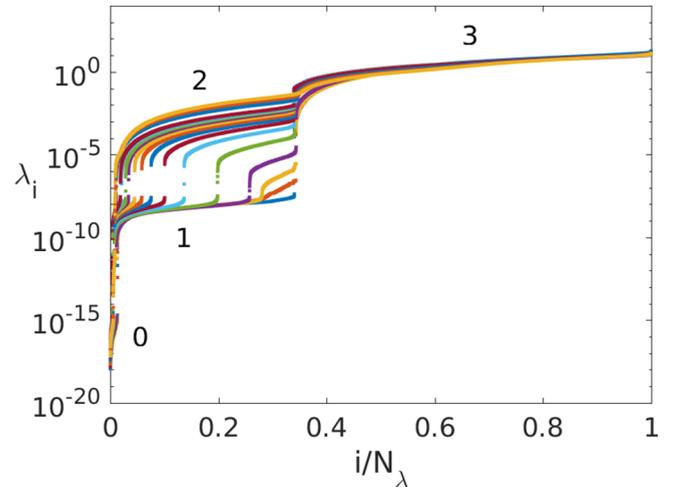

FIG. 7. The eigenvalues λ_i of the dynamical matrix sorted from smallest to largest for static packings of $N = 100$ circulo-lines at the 17 different asphericities $\mathcal{A} - 1$ shown in Fig. 6 ranging from $\approx 10^{-6}$ to 1 and decreasing from top to bottom. $N_\lambda = 15\,000$ is the total number of eigenvalues in all of the packings at a given asphericity. For each asphericity (different colors), we show spectra for 50 separate packings. We label four distinct regions of the eigenvalue spectra, 0–3. Region 0 ($\lambda_i \lesssim 10^{-14}$) corresponds to unconstrained degrees of freedom (such as overall translations due to periodic boundary conditions, rattler and slider particles), region 1 ($10^{-14} \lesssim \lambda_i \lesssim 4 \times 10^{-8}$) corresponds to "quartic modes," whose number is determined by the number of missing contacts relative to the isostatic contact number, region 2 corresponds to eigenmodes with predominantly rotational motion, and region 3 corresponds to eigenmodes with predominantly translational motion.

$\mathcal{A} - 1$, the coordination number for packings of circulo-lines and circulo-polygons, as well as ellipses, approaches $\langle z \rangle = 4$, which is expected for bidisperse disk packings. At large asphericities, $\langle z \rangle = 6$ for packings of circulo-lines and circulo-polygons as expected for isostatic packings with two translational and one rotational degree of freedom per particle. $\langle z \rangle$ for ellipse packings plateaus for large $\mathcal{A} - 1$. However, the current data suggest that the plateau value is less than 6, indicating that ellipse packings are hypostatic for all $\mathcal{A} - 1$.

An interesting feature in $\langle z \rangle (\mathcal{A})$ for static packings of circulo-lines and circulo-polygons is the plateau in $\langle z \rangle$ that occurs near $\mathcal{A} - 1 \approx 10^{-5}$ in Fig. 8. Our results suggest that the plateau is likely an artifact of the small, but nonzero pressure of the static packings. If the particles are overcompressed, even slightly, nearly parallel contacts will be able to exert larger torques than they would at zero pressure, which causes more eigenvalues to be above the eigenvalue threshold λ_c, and contacts to be counted as two constraints instead of one. Thus, as we decrease the pressure to zero, we expect to count fewer of these nearly parallel contacts as two constraints and the plateau in $\langle z \rangle$ near $\mathcal{A} - 1 \approx 10^{-5}$ will decrease. As $\mathcal{A} - 1$ decreases below 10^{-5}, the effects from overcompression are less important, and the nearly parallel contacts are only counted once.

In Fig. 9, we plot the eigenvalues λ_i sorted from smallest to largest for static packings of five different particle shapes (circulo-lines, circulo-triangles, circulo-pentagons,
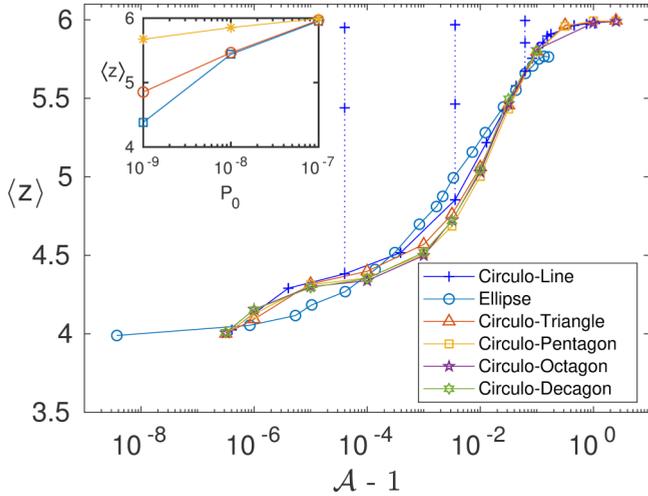
FIG. 8. The average coordination number $\langle z \rangle$ [Eq. (3)] at jamming onset is plotted versus asphericity $\mathcal{A} - 1$ for packings of $N = 100$ circulo-lines (plus signs), circulo-triangles (triangles), circulo-pentagons (squares), circulo-octagons (five-pointed stars), and circulo-decagons (six-pointed stars). These data are compared to $\langle z \rangle$ for packings of $N = 480$ ellipses (circles). For packings of circulo-lines and circulo-polygons, we define $\langle z \rangle$ using $N_c = N_c^0 - N_1$. In the inset, we show $\langle z \rangle$ as a function of pressure P_0 for packings of circulo-lines for $\mathcal{A} - 1 = 4 \times 10^{-5}$ (squares), 3.6×10^{-3} (circles), and 6.2×10^{-2} (asterisks). $\langle z \rangle$ decreases more rapidly with P_0 at lower asphericities. All data points in the inset are also plotted in the main figure using plus signs connected by dotted lines.

circulo-octagons, and circulo-decagons) at the same asphericity, $\mathcal{A} = 1.1$. We find that the eigenvalue spectra for all of these shapes are nearly identical. This behavior differs markedly from that in Fig. 7, where we show the eigenvalue spectra for packings with the same particle shape (circulo-lines), but
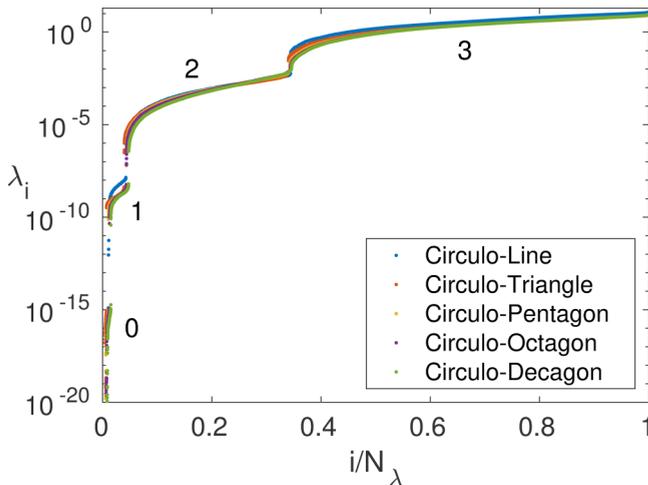

FIG. 9. The eigenvalues i of the dynamical matrix sorted from smallest to largest for static packings of $N = 100$ circulo-lines (blue), circulo-triangles (red), circulo-pentagons (yellow), circulo-octagons (purple), and circulo-decagons (green) at asphericity $\mathcal{A} = 1.1$. $N_\lambda = 15\,000$ is the total number of eigenvalues in all of the packings of a given shape. For each particle shape, we show spectra for 50 separate packings. Regions 0–3 are defined the same way as in Fig. 7.
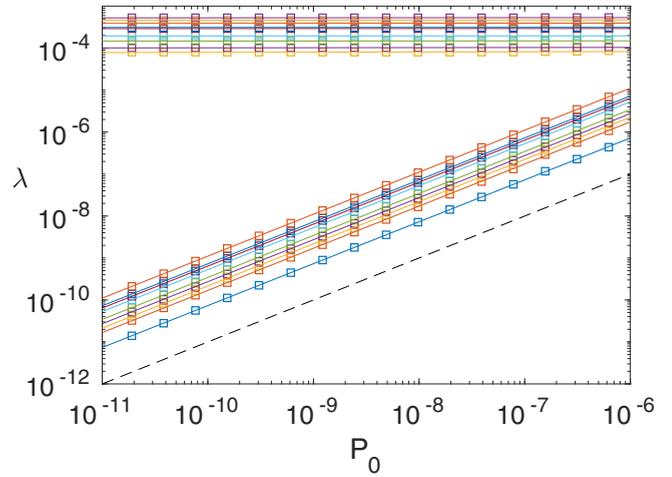

FIG. 10. Nine eigenvalues λ of the dynamical matrix from regions 1 (bottom) and 2 (top) plotted versus pressure P_0 for a static packing of $N = 32$ circulo-lines with asphericity $\mathcal{A} = 1.03$. The dashed line has slope 1.

at different values of the asphericity. Circulo-polygons with n sides possess $2n - 3$ parameters that specify their shape (not counting uniform scaling of lengths). Our results suggest that asphericity is a key parameter in determining the structure, geometry, and physical properties of hypostatic packings.

The reason why the eigenvalues in region 1 (cf. Fig. 7) are referred to as "quartic modes" is that, for perturbations along the corresponding eigenvectors, the total potential energy scales quartically with the amplitude of the perturbation, rather than quadratically, as one would expect for mechanically stable packings [5,6]. In Fig. 10, we plot eigenvalues from regions 1 and 2 as a function of pressure P_0 for a static packing of $N = 32$ circulo-lines at asphericity $\mathcal{A} = 1.03$. The eigenvalues from region 2 are independent of pressure, whereas the eigenvalues from region 1 scale linearly with pressure. Thus, for packings of circulo-lines and other particle shapes that yield hypostatic packings, the eigenvalues corresponding to the quartic modes are zero at jamming onset ($P_0 = 0$). This result agrees with prior studies of hypostatic packings of ellipses and ellipsoids [6].

For hypostatic packings, perturbations along the quartic modes are constrained to fourth order. In Fig. 11, we show the fourth derivatives of the total potential energy $d^4 U / d\vec{\lambda}^4$ in the directions of the nine eigenmodes in region 1 (that are depicted near the bottom of Fig. 10). We find that the fourth derivatives along eigenmodes in region 1 do not depend on pressure, and thus remain nonzero at zero pressure. These findings demonstrate that hypostatic packings are fully constrained at zero pressure, in some directions by quadratic potentials and in other directions by quartic potentials.

C. Convex versus concave constraints

Why are hypostatic packings of circulo-lines and other nonspherical particles mechanically stable when they possess fewer contacts than the isostatic number, $N_c < N_c^0$? We have already shown that the number of missing contacts $N_c^0 - N_c$ matches the number of quartic modes along which the energy increases quartically, not quadratically, with the perturbation
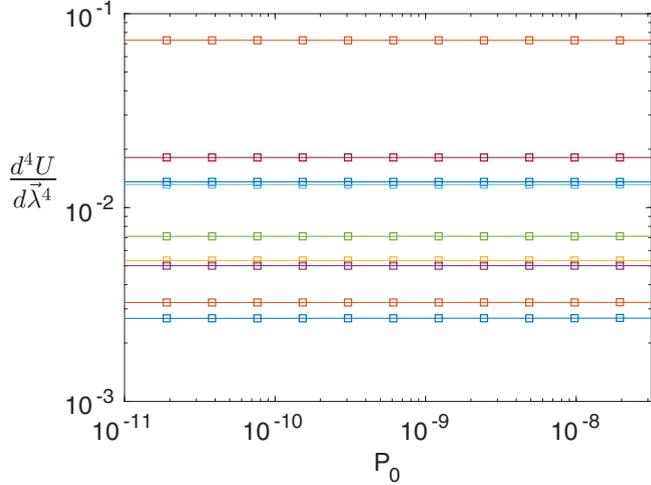
FIG. 11. For the same packing as in Fig. 10, we plot the fourth derivative of the total potential energy $d^4U/d\vec{\lambda}^4$ in the direction of the nine eigenmodes in region 1 in the bottom of Fig. 10 as a function of pressure P_0. All of the fourth derivatives for the region 1 eigenmodes are independent of pressure.
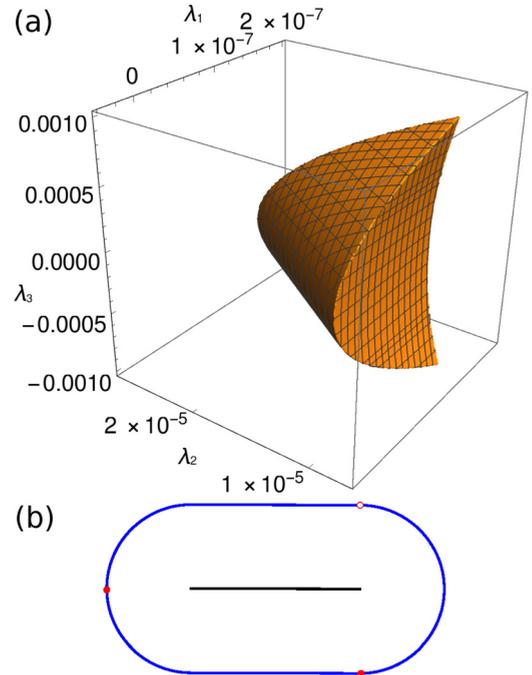

FIG. 12. (a) Depiction of the feasible region of configurations that do not possess interparticle overlaps for a single circulo-line surrounded by three fixed points as shown in (b). This system is generated by fixing three points in space, initializing a circulo-line between the three points, and growing the interior circulo-line until it reaches force and torque balance while in contact with the three points. After finding the stable configuration, we decrease the diameter of the interior circulo-line by 10^{-7}. The extent of the feasible region is shown using coordinates along the the three eigendirections ($\vec{\lambda}_1$, $\vec{\lambda}_2$, and $\vec{\lambda}_3$) of the dynamical matrix for the interior circulo-line. The top contact (open circle) in (b), which is positioned along the shaft of the circulo-line, provides the constraint with convex curvature.

amplitude. In the other N_c eigendirections of the dynamical matrix, the energy increases quadratically with the perturbation amplitude. As a result, there are no directions in configuration space for which these hypostatic packings can be perturbed without energy cost, and thus they are mechanically stable.

To more fully address the question of how hypostatic packings of nonspherical particles can be mechanically stable, we consider the so-called "feasible region" of configuration space near each static packing for packing fractions slightly below jamming onset [4]. The feasible region near a given static packing includes all configurations for which there are no particle overlaps. The boundaries of this region are determined by all of the interparticle contacts, each of which corresponds to an inequality among the particle coordinates specifying when pairs of particles do not overlap. Points in configuration space that satisfy all of the inequalities are inside the feasible region. For mechanically stable packings, as the packing fraction is increased, the feasible region shrinks and becomes bounded and compact, preventing particle rearrangements that would allow the system to transition to a different packing. A static packing is mechanically stable if the feasible region of accessible configurations shrinks to a single point at jamming onset.

The number of constraints required to bound the feasible region depends on the curvature of the inequality constraints in configuration space, i.e., whether the constraints are concave or convex [4]. The inequality constraints that arise in disk packings are always concave. In particular, in disk packings, the curvature of each constraint is equal to minus the reciprocal of the sum of the radii of the two disks in contact. As a result, the number of contacts required to bound the feasible region for a mechanically stable packing of N disks is $2N + 1$ (minus 2 from overall translations in periodic boundary conditions). Thus, *hypostatic* packings of nonspherical particles must possess contacts that give rise to bounding surfaces with convex curvature, which allows packings to be mechanically stable with fewer than the isostatic number of contacts.

In Fig. 12, we show a simple configuration involving a circulo-line that gives rise to a convex constraint. We consider three points at fixed positions. These points represent less strict constraints than contacts with other circulo-lines and, thus, if these three points can constrain a circulo-line, three contacting circulo-lines will constrain an interior circulo-line as well. We initialize a circulo-line at several locations between the three points, and then increase the size of the interior circulo-line until it is constrained by the three points. After the circulo-line is constrained, we shrink its diameter by 10^{-7} so that it no longer overlaps the bounding points. The feasible region of the slightly undercompressed circulo-line is shown in Fig. 12(a).

For an isostatic system, four contacts are required to constrain a circulo-line. However, we find configurations in which a circulo-line is constrained by only three contacts. Figure 12(a) illustrates the reason that only three contacts are necessary: one of the contacts (open circle on the top shaft) gives rise to a constraint with convex curvature in configuration space. In contrast, the other two contacts (filled circles), which are on the end caps of the circulo-line, give rise to constraints with concave curvature. This example suggests that only certain types of contacts between circulo-lines generate constraints with convex curvature, and thus the number of
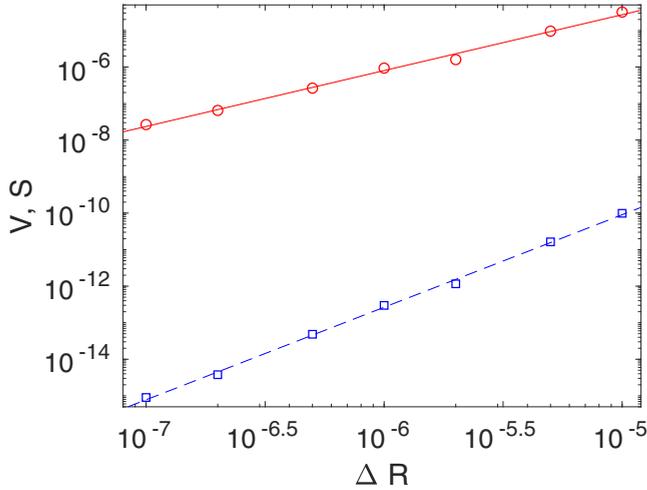
FIG. 13. The volume V (squares) and surface area S (circles) of the feasible region in Fig. 12(a) plotted as a function of the decrease in radius $\Delta R = R_j - R$, where R_j is the radius at which the system is fully constrained. The solid and dashed lines have slopes 2.5 and 1.5, respectively.

contacts required for mechanical stability is less than the isostatic number when these types of contacts are present.

To verify that the circulo-line "packing" in Fig. 12(b) is mechanically stable, we numerically calculated the volume V and surface area S of the feasible region as a function of the degree of undercompression, $\Delta R = R_j - R$, where R_j is the radius of the interior circulo-line at which the system is jammed. In Fig. 13, we show that both V and S display power-law scaling with ΔR, emphasizing that the feasible region for hypostatic packings shrinks to a point at jamming onset, and thus these packings are mechanically stable.

To further investigate the effect of convex and concave constraints on a hypostatic jammed packing, we measured the curvatures of the inequality constraints for each contact in a static packing with $N = 24$ bidisperse circulo-lines with asphericity $\mathcal{A} = 1.04$. We classified the contacts into five types as defined in Appendix A. Parallel contacts can involve the shaft of one circulo-line (middle) and the end cap of another (end). This arrangement gives rise to two types of contacts, one for the circulo-line with a contact on its end and another

for the circulo-line with a contact on its middle. Similarly, the shaft (middle) of one circulo-line can be in contact with the end cap (end) of another, but the long axes are not parallel. This arrangement again gives rise to two types of contacts, one for the circulo-line with a contact on its end and another for the circulo-line with a contact on its middle. In addition, the ends of two circulo-lines can be in contact.

The average curvatures and standard errors from the root-mean-square deviations from the average of the bounding surfaces for each contact type in a static packing of $N = 24$ bidisperse circulo-lines with $\mathcal{A} = 1.04$ are compiled in Table II. (We find similar mean values and errors when we average over an ensemble of 100 static packings composed of $N = 24$ bidisperse circulo-lines with $\mathcal{A} = 1.04$.) We find that the standard errors in the principal curvatures for all contact types (except the error for $\langle \kappa_2 \rangle$ for particles whose end is in parallel contact, which is 17%) are on the order of 1% or less. Hence, (for small $\mathcal{A}$) each contact type has a well-defined range of curvatures associated with it. Also, our preliminary studies show that, when increasing system size by a factor of 4, the standard deviations of the curvature distributions for all contact types *decrease* by roughly a factor of 2, except for the distribution of κ_2 for parallel (end-particle) contacts, which increases by $\sim 60\%$, and κ_1 for end-end contacts, which increases by a factor of 2. However, both of these types of contacts correspond to nonconvex constraints in configuration space. As a result, the increasing width of these distributions does not significantly impact whether a hypostatic packing is mechanically stable in large systems. In contrast, when the asphericity of the particle shape is increased, the contact curvature distribution for most of the contact types becomes proportionally wider. This result may be related to the fact that packings with large asphericity approach isostaticity, though further research is required to understand this correlation.

From these data, we can draw several conclusions about the contribution of each type of contact to the stability of circulo-line packings. First, end-end contacts yield concave constraints in configuration space, and thus on their own do not give rise to mechanically stable hypostatic packings. In contrast, end-middle contacts have a positive principal curvature for the circulo-line whose middle is in contact, and thus serve to stabilize hypostatic packings. Parallel contacts also possess a positive curvature associated with the circulo-line whose

TABLE II. The principal curvatures ($\langle \kappa_1 \rangle$ and $\langle \kappa_2 \rangle$) and standard errors (given by the root-mean-square deviations from the average) for the different types of contacts that can occur between two circulo-lines in a $N = 24$ packing of bidisperse circulo-lines with asphericity $\mathcal{A} = 1.04$, averaged over all contacts in the packing of that type. We calculated $\kappa_1 = 0$ for parallel (end-particle) contacts and $\kappa_2 = 0$ for end-middle (end-particle) contacts analytically, so the standard errors are not provided for those contact types. Note that for κ_2 for an end particle in a parallel contact, the magnitude of the curvature was averaged, rather than the signed curvature because, unlike any of the other curvatures, this one fluctuated between positive and negative. This type of averaging is denoted using an asterisk.

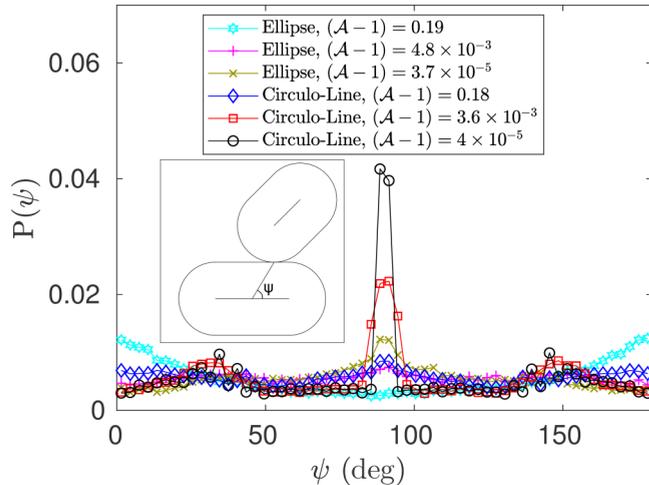| Contact type	$\langle \kappa_1 \rangle$	$\langle \kappa_2 \rangle$
Parallel (end particle)	0	$(*)(7.93 \pm 1.40) \times 10^{-9}$
Parallel (middle particle)	-1.292 ± 0.005	0.774 ± 0.003
End-middle (end particle)	-0.0261 ± 0.0004	0
End-middle (middle particle)	-1.292 ± 0.002	0.774 ± 0.001
End-end	-5.69 ± 0.01	-0.0246 ± 0.0002

FIG. 14. Probability distribution $P(\psi)$ of the contact angles ψ in bidisperse ellipse ($N = 480$) and circulo-line ($N = 100$) packings at several asphericities: ellipses at $\mathcal{A} - 1 = 0.19$ (six-pointed stars), 5×10^{-3} (plus signs), and 4×10^{-5} (exes), and circulo-lines at $\mathcal{A} - 1 = 0.18$ (diamonds), 4×10^{-3} (squares), and 4×10^{-5} (circles). In the inset, we define the contact angle ψ as the angle between the shaft of a circulo-line and the vector pointing from its center to the point of contact with another circulo-line. We use a similar definition for the contact angle for ellipses. Packings of circulo-lines, as well ellipses, favor parallel contacts, even at small asphericities.

middle is in contact. However, note that the concave curvature for circulo-lines whose end is in *parallel* contact is much smaller than the concave curvature of the end circulo-line for end-middle contacts. This means that for circulo-lines with end contacts, the parallel contacts are more "stabilizing" than the end-middle contacts, and therefore they occur more frequently in mechanically stable hypostatic circulo-line packings than other end-middle contacts.

The above observations about the curvatures of the inequality constraints in configuration space can help explain the distribution of contact angles $P(\psi)$ in static packings of elongated particles [38,39] shown in Fig. 14. This figure shows that, even for packings of circulo-lines at very small asphericities, parallel contacts are highly probable, despite the fact that the range of angles for parallel contacts at low asphericities is small. This behavior for $P(\psi)$ can be explained by the fact that end-middle and parallel contacts can contribute to making a hypostatic packing mechanically stable, whereas end-end contacts cannot. (See Table II.) Thus, end-middle and parallel contacts (whose contact angles are close to $90°$ at low asphericities) must be present to stabilize hypostatic packings of low-asphericity circulo-lines. As shown in Fig. 14, $P(\psi)$ is similar for both ellipse and circulo-line packings.

IV. CONCLUSIONS AND FUTURE DIRECTIONS

In this article, we carried out computational studies of static packings of frictionless nonspherical particles in 2D. We developed an interparticle potential for circulo-lines and circulo-polygons that generates continuous and differentiable pair forces and torques as a function of the particle coordinates. As a result, we are able to compare the structural and

mechanical properties of mechanically stable packings of nine different nonspherical particle shapes: circulo-lines, circulo-triangles, circulo-pentagons, circulo-octagons, and circulo-decagons, asymmetric dimers, dumbbells, Reuleaux triangles, and ellipses. Our studies place a particular emphasis on the question of which particle shapes give rise to *hypostatic* mechanically stable packings with fewer contacts than the isostatic number.

We conjecture that to form hypostatic mechanically stable packings, strictly and effectively convex, frictionless particles must satisfy the following two criteria: (i) the particle has one or more nontrivial rotational degrees of freedom, and (ii) the accessible (nonexcluded) contact area cannot be achieved by a union of a finite number of disks. If the particle does not satisfy both criteria, we expect it to form isostatic packings. Packings of the nine particle shapes we considered are consistent with this conjecture. Future research can investigate methods to analytically prove this conjecture [40].

We then studied the packing fraction ϕ and coordination number z at jamming onset for packings of a number of different types of nonspherical shapes in 2D as a function of asphericity $\mathcal{A}$. To do this, we resolved the ambiguity in the constraint counting of nearly parallel contacts of circulo-lines and circulo-polygons using the branched structure of the eigenvalue spectra of the dynamical matrix. In future research, we will study the coordination number of packings of sphero-cylinders and sphero-polygons in 3D, and compare the results to those in 2D, since it is extremely unlikely for sphero-cylinders and sphero-polyhedra to form nearly parallel contacts along their edges.

We find that the packing fraction and coordination number of hypostatic packings obey approximate master curves when plotted versus the asphericity. This result agrees qualitatively with prior studies, which find that the coordination number increases with the isoperimetric quotient (that is similar to asphericity) in crystalline packings of polyhedra [41,42]. Further, the eigenvalue spectra for different particle shapes, at the same $\mathcal{A}$, collapse. These results suggest that asphericity is a key parameter in determining the structure, geometry, and mechanical properties of hypostatic packings. Other studies [43] have shown that the second virial coefficient in the equation of state for hard particle fluids is a linear function of the particle asphericity. This result is consistent with the collapse of the packing fraction and coordination number at jamming onset onto a master curve when plotted against the asphericity. For n-sided circulo-polygons, there are $2n - 3$ parameters that specify their shape. In future studies, we will investigate additional shape parameters, such as the ratios of the area moments and others [44], to better understand the coupling between the wide shape parameter space and the properties of hypostatic packings of nonspherical particles.

We also demonstrated that hypostatic packings of circulo-lines (and by analogy circulo-polygons) are mechanically stable by showing that even though the eigenvalues of the dynamical matrix for the quartic modes tend to zero at zero pressure, the fourth derivatives of the total potential energy in the directions of the quartic modes do not. Thus, hypostatic packings of nonspherical particles are stable to perturbations in all directions in configuration space. Perturbations in some directions give rise to quadratic potentials, whereas other
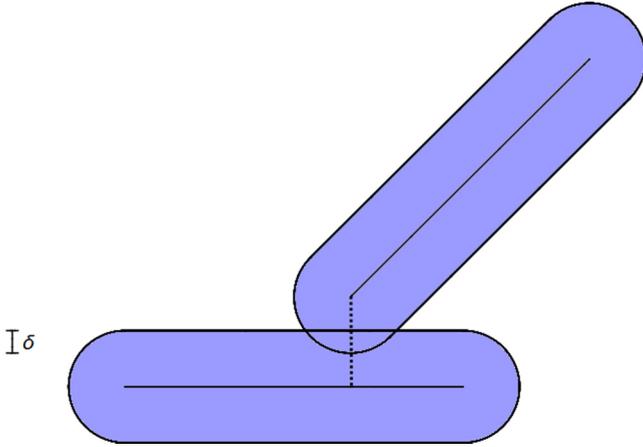
FIG. 15. A contact between the end cap of one circulo-line and the middle of another. The separation between the circulo-lines r_{ij} is indicated by the dotted line between the circulo-line shafts. The separation vector $\vec{r}_{ij}$ connects the end of the shaft of one circulo-line to the shaft of the other and is perpendicular to shaft of the circulo-line with the middle contact. The overlap is defined as $\delta = \sigma_{ij} - r_{ij}$, where σ_{ij} is the sum of the end cap radius and the half-width of the shaft it overlaps.

directions give rise to quartic potentials. In the directions with quartic potentials, we expect large anharmonic contributions to the vibrational and mechanical response [45].

In addition, we measured the curvatures of the inequality constraints that arise from interparticle contacts in hypostatic packings of circulo-lines to better understand the grain-scale mechanisms that allow hypostatic packings to be mechanically stable. The contacts in isostatic disk packings give rise to inequality constraints with only concave (negative) curvatures. In contrast, hypostatic packings of circulo-lines (and other nonspherical particles) possess different types of contacts (e.g., end-end and end-middle). Some types yield inequality constraints with concave curvatures and others yield inequality constraints with convex curvatures. We find that contacts with convex inequality constraints are present even at small asphericities. The contacts with convex inequality constraints allow the feasible region of slightly undercompressed hypostatic packings to be compact, bounded, and shrink to zero in the limit that the free volume tends to zero. In future research, we will investigate whether a generalization of the isocounting conjecture to nonspherical particles can be derived based on these findings.
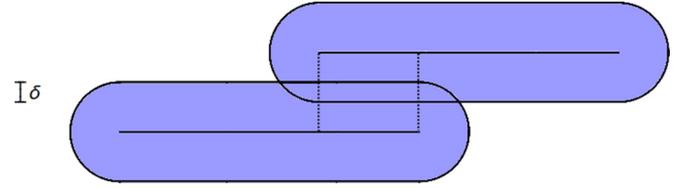
FIG. 16. When two circulo-lines possess a parallel contact, it is counted twice, as two end-middle contacts. The separations r_{ij} are depicted by the vertical dotted lines between the circulo-line shafts, and $\vec{r}_{ij}$ points from the end of one of the shafts to the other and is perpendicular to the shafts. The overlap is given by $\delta = \sigma_{ij} - r_{ij}$ for both contacts, where σ_{ij} is the sum of the end cap radius and the half-width of the shaft it overlaps.

APPENDIX A: CONTINUOUS POTENTIAL BETWEEN CIRCULO-LINES AND CIRCULO-POLYGONS

The interparticle potential we implement is similar to others used for simulations of faceted and sphero-polyhedral particles [29–33]. However, we made several adjustments to the potential to handle transitions between different types of contacts to ensure continuity and differentiability.

The repulsive potential between two circulo-lines is given by Eq. (1), where r_{ij} is the magnitude of $\vec{r}_{ij}$, which points from the location where the force is applied on circulo-line j to the location where the force is applied on circulo-line i. These points of contact can be located on the ends or the shaft (middle) of a circulo-line. In this appendix, we define the overlap distance $\delta = \sigma_{ij} - r_{ij}$, which will depend on the type of contact that occurs between two circulo-lines.

1. Types of contacts

There are three general types of interparticle contacts that occur in packings of circulo-lines: (1) the end of one circulo-line is in contact with the middle of another (Fig. 15), (2) the shafts of two circulo-lines are in contact and the circulo-lines are nearly parallel (Figs. 16 and 17), and (3) the ends of two circulo-lines are in contact (Fig. 18). Below, we define the overlap distance δ in the circulo-line potential [Eq. (1)] for each type of contact.
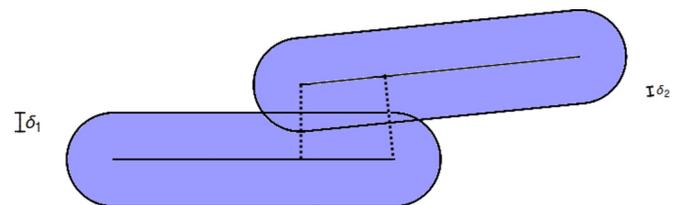

FIG. 17. When the shafts of two contacting circulo-lines are close to parallel, such that both end caps overlap the shaft of the other circulo-line, the contact is counted twice as for parallel contacts. Each separation vector $\vec{r}_{ij}$ (depicted by dotted lines between circulo-line shafts) points from the end of the shaft of the circulo-line with an end contact to the shaft of the circulo-line with the middle contact, and is perpendicular to the shaft of the circulo-line with the middle contact. The overlaps are given by $\delta_{1,2} = \sigma_{ij} - r_{ij}$ for the two contacts with different separations, where σ_{ij} is the sum of the end cap radius and the half-width of the shaft it overlaps.
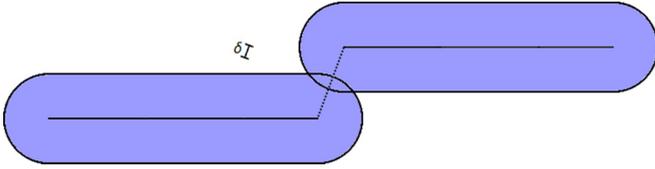
FIG. 18. An end-end contact between the end caps of two circulo-lines. The separation $\vec{r}_{ij}$ between circulo-lines (dotted line) gives the distances between the ends of the shafts of the two circulo-lines. The overlap is given by $\delta = \sigma_{ij} - r_{ij}$, where σ_{ij} is the sum of the radii of the end caps.

a. End-middle contacts

End-middle contacts occur when the end cap of one circulo-line makes contact with the middle of another circulo-line, but does not overlap with either of the other circulo-line's end caps. (See Fig. 15.) In this case, we assume that the separation vector $\vec{r}_{ij}$ between circulo-lines points from the end of the shaft of the circulo-line with the end contact to the shaft of the other circulo-line. $\vec{r}_{ij}$ is perpendicular to the shaft of the circulo-line with the middle contact. The overlap between circulo-lines with an end-middle contact is $\delta = \sigma_{ij} - r_{ij}$, as shown in Fig. 15.

b. Parallel and nearly parallel contacts

For parallel and nearly parallel contacts, an end cap of both circulo-lines overlaps the shaft of the other circulo-line. In this case, the spring potential in Eq. (1) for both overlaps is calculated as for end-middle contacts. If the circulo-lines are parallel, as in Fig. 16, $\delta = \sigma_{ij} - r_{ij}$ is the same for both overlaps. However, for nearly parallel contacts, as in Fig. 17, the separations are different for the two end-middle overlaps. This method for treating end-middle, parallel, and nearly parallel contacts ensures continuity and differentiability of the potential as a function of the particle coordinates. If the circulo-lines in Fig. 17 rotate until their orientations match Fig. 15, the potential, force, and torque must all change continuously. Using our method, δ_2 decreases continuously to zero as the contact evolves from that in Fig. 17 to that in Fig. 15. In addition, δ_1 decreases continuously to zero as the circulo-lines in Fig. 17 rotate until δ_2 is the only overlap.

c. End-end contact

Also, suppose that we slide the two circulo-lines in Fig. 16 away from each other until they are similar to the configuration in Fig. 18 and form an end-end contact. In this case, we assume that the two overlap potentials add together as soon as the two relevant ends of the circulo-line shafts slide past each other. Therefore, to ensure continuity, the interaction potential for an end-end contact must be twice as large as that for an end-middle contact. Hence, we use $U = k\delta^2$ for end-end contacts.

However, this treatment of end-end contacts creates a discontinuity for the configuration in Fig. 19. If we imagine sliding the circulo-lines past each other until the overlap δ_1 is associated with an end-end contact, the potential will suffer a discontinuous jump from $\frac{1}{2}k\delta_1^2$ to $k\delta_1^2$ since the end-end contact potential is twice as large as an end-middle potential. To remedy this discontinuity, we add the end-end contact potential
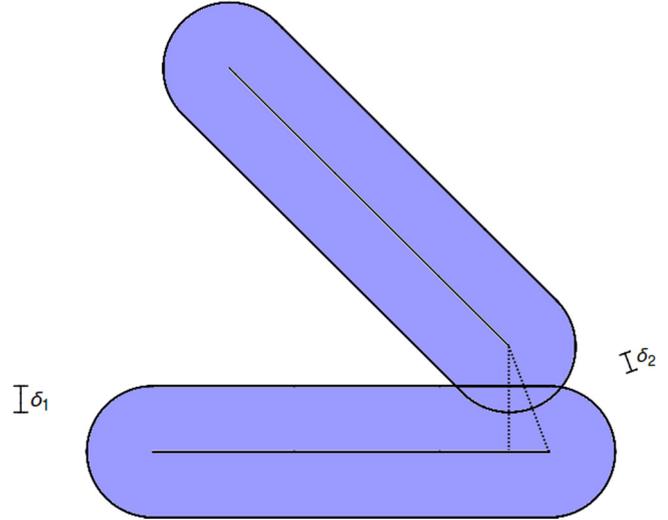

FIG. 19. When a contact between circulo-lines is close to the boundary between the end of one and middle of another circulo-line, we include both the end-end and end-middle overlaps to ensure continuity as the contact crosses the boundary. The separation vector $\vec{r}_{ij}$ associated with the end-middle overlap δ_1 (vertical dotted line) points from the end of the shaft of one circulo-line to the shaft of the other, such that it is perpendicular to the shaft. The separation vector associated with the end-end overlap δ_2 (diagonal dotted line) points from the end of the shaft of one of the circulo-lines to the end of the shaft of the other overlapping circulo-line.

between the two relevant end points as soon as they become close enough to overlap. However, we do not make the end-end potential twice as large in this case. Hence, the potential in this case is given by $U = \frac{1}{2}k(\delta_1^2 + \delta_2^2)$. Thus, when we perform that same sliding transformation, the potential will grow continuously from $\frac{1}{2}k\delta_1^2$ to $k\delta_1^2$ as δ_2 grows continuously from 0 to δ_1. Note that we do not add this end-end overlap potential if two end-middle contacts are present, as in Fig. 20, because in that case, the potential will already change continuously as
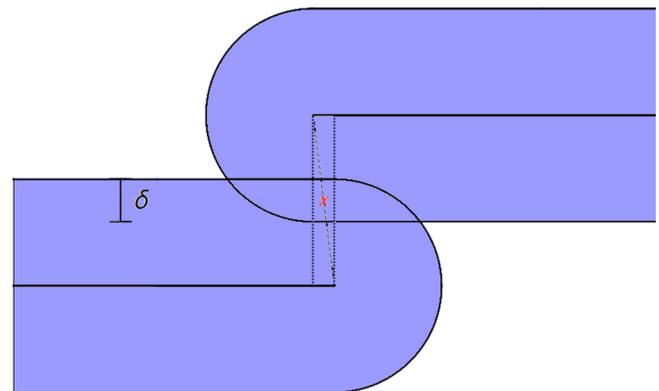

FIG. 20. We do not calculate the end-end overlap potential for parallel and nearly parallel circulo-lines since this would lead to a discontinuity if the configuration transitions to an end-end contact by sliding. Instead, we choose the circulo-line separations for parallel and nearly parallel contacts as shown in Fig. 16. The separation associated with an end-end contact is indicated by the dashed line with an x in the middle.
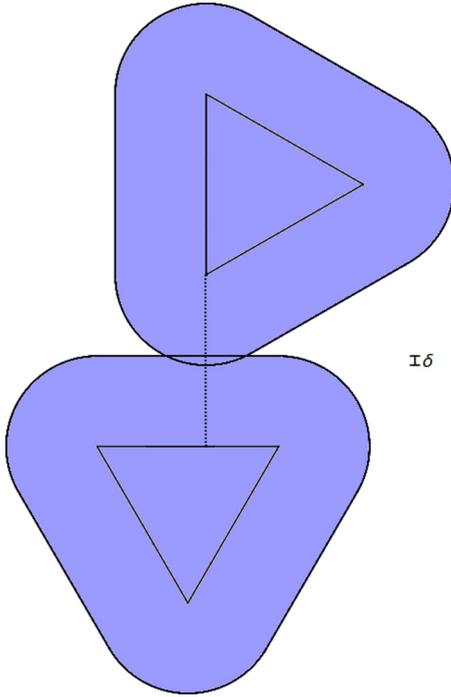
FIG. 21. A schematic of an end-middle contact between two circulo-triangles. The separation r_{ij} between circulo-triangles (dotted line) is given by the perpendicular distance between the vertex of the circulo-triangle with the end contact and the side of the closest side of the triangle in the circulo-triangle with the middle contact. The overlap $\delta = \sigma_{ij} - r_{ij}$, where σ_{ij} is the sum of the end cap radius and half-width of the shaft it overlaps.

described in the previous subsection, and hence there is no discontinuity to remedy.

2. Generalizing the circulo-line potential to circulo-polygons

Generalizing our continuous circulo-line potential to circulo-polygons, such as those pictured in Fig. 21, is straightforward. We simply calculate the potential between all pairs of circulo-lines that comprise each circulo-polygon. For example, in Fig. 21, since the vertex of the top circulo-triangle is shared by two circulo-lines, we count the end-middle contact twice, and hence the overlap potential is $U = k\delta^2$.

APPENDIX B: GENERATION OF CIRCULO-POLYGONS

A circulo-polygon is formed through a Minkowski sum of a polygon and a disk with a radius r [46], which is equivalent to the sweeping of the disk around the profile of the polygon as in Fig. 22(a). The shape of a circulo-polygon with n edges is fully specified by $2n - 3$ independent parameters. In this work, we focus on the asphericity shape parameter $\mathcal{A}$, which measures the deviation of a given shape from a circle in 2D.

We study bidisperse packings of circulo-polygons with asphericity $\mathcal{A}$ for which half of the circulo-polygons are large and half are small. The large circulo-polygons have areas that satisfy $a_L = 1.4^2 a_S$, where $a_{L,S}$ is the area of the large and small circulo-polygons, respectively. The large circulo-polygons (and small ones) have different shapes at the same
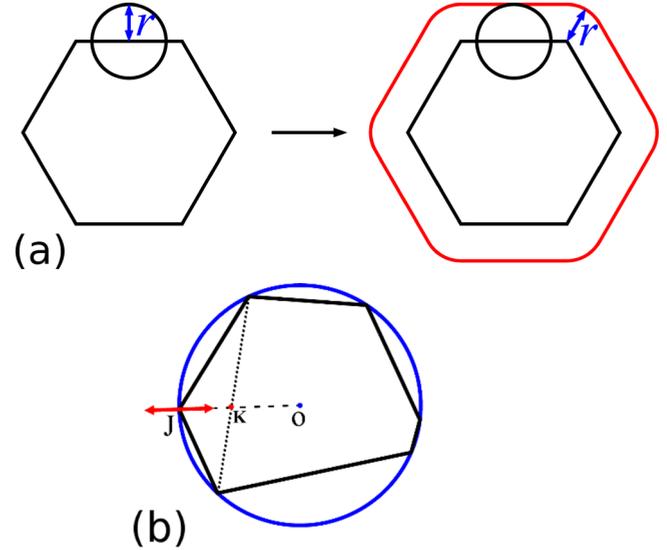

FIG. 22. (a) A circulo-polygon is the Minkowski sum of a polygon (e.g., the regular hexagon on the left) and a disk with radius r, which is "swept" along the edges of the polygon to form the circulo-polygon (the red shape on right). (b) Schematic of the generation of a circulo-polygon at a given asphericity $\mathcal{A}$. First, we select n random points on a unit circle (blue curve) with origin O (where n is the desired number of edges). We then randomly choose vertex J and either stretch or shorten the distance between J and O (dashed line) by an amount randomly chosen between 0 and the distance JK to adjust $\mathcal{A}$ to match the target asphericity.

$\mathcal{A}$. We generate different circulo-polygons at the same $\mathcal{A}$ using the following two-step approach: (1) We first randomly select n points on a unit disk as the vertices of an n-sided polygon. The radius r of the circulo-polygon is set to be n percent of the perimeter of the polygon. (2) If the asphericity of the current circulo-polygon is smaller than the target $\mathcal{A}$, a vertex J is randomly chosen and then stretched or shortened along the direction between the vertex J and the center O of the unit disk, by a distance randomly chosen between 0 and the distance between J and the intersection of JO with the line segment connecting the two neighboring vertices, as shown in Fig. 22(b). This deformation is accepted only if the asphericity of the new shape is closer to $\mathcal{A}$ than the original and the new shape is still effectively convex. If the asphericity of the current circulo-polygon exceeds $\mathcal{A}$, the radius r is increased to match the target $\mathcal{A}$. We repeat step 2 until a circulo-polygon with $\mathcal{A}$ is obtained.

APPENDIX C: DYNAMICAL MATRIX ELEMENTS OF CIRCULO-POLYGON PACKINGS

In this Appendix, we provide explicit expressions for the dynamical matrix elements for static packings of circulo-polygons that interact via the purely repulsive linear spring potential in Eq. (1). In this expression, R_i is radius that forms the edge of circulo-polygon i and $\vec{r}_{ji}$ is the separation vector from circulo-polygon i to j, which is is given by

$$\vec{r}_{ji} = \vec{c}_{ji} + \mathcal{R}_j \vec{v}_n - \mathcal{R}_i \vec{v}_m + \mathcal{R}_j \hat{u}_n l_n - \mathcal{R}_i \hat{u}_m l_m, \quad \text{(C1)}$$

where $\vec{c}_{ji} = (x_j - x_i, y_j - y_i) \equiv (p, q)$ is the center-to-center separation between circulo-polygons, $\mathcal{R}_i = \begin{bmatrix} \cos\theta_i & -\sin\theta_i \\ \sin\theta_i & \cos\theta_i \end{bmatrix}$ is the rotation matrix in 2D, θ_i is the orientation of particle i relative to the x axis, $\vec{v}_m$ is the vector from the center of particle i to the center of its corresponding edge m when particle i at zero rotation, $\hat{u}_m$ is the unit vector along edge m at zero rotation, and l_m indicates the distance between the contact point and the center of edge m.

The dynamical matrix requires the calculation of the second derivatives of the total potential energy U, and can be expressed in terms of the first and second derivatives of the contact distance r_{ji} with respect to the particle coordinates:

$$\frac{\partial^2 U}{\partial \xi_i \partial \xi_j} = \frac{\partial r_{ji}}{\partial \xi_i} \frac{\partial r_{ji}}{\partial \xi_j} - (\sigma_{ji} - r_{ji}) \frac{\partial^2 r_{ji}}{\partial \xi_i \partial \xi_j}, \qquad \text{(C2)}$$

where $\xi_i = x_i, y_i,$ or θ_i,

$$\frac{\partial r_{ji}}{\partial \xi_i} = \frac{\vec{r}_{ji}}{r_{ji}} \cdot \frac{\partial \vec{r}_{ji}}{\partial \xi_i}, \qquad \text{(C3)}$$

and

$$\frac{\partial^2 r_{ji}}{\partial \xi_i \partial \xi_j} = \frac{1}{r_{ji}} \left(\frac{\partial \vec{r}_{ji}}{\partial \xi_i} \cdot \frac{\partial \vec{r}_{ji}}{\partial \xi_j} + \vec{r}_{ji} \cdot \frac{\partial^2 \vec{r}_{ji}}{\partial \xi_i \partial \xi_j} - \frac{\partial r_{ji}}{\partial \xi_i} \frac{\partial r_{ji}}{\partial \xi_j} \right). \qquad \text{(C4)}$$

There are two types of contacts among circulo-polygons. The first type is a vertex-to-edge contact. Assuming the end point of edge n on particle j is in contact with edge m on particle i, l_n is half of the length of edge n, and l_m can be written as

$$l_m = (\vec{c}_{ji} + \mathcal{R}_j \vec{v}_n - \mathcal{R}_i \vec{v}_m + \mathcal{R}_j \hat{u}_n l_n) \cdot \mathcal{R}_i \vec{u}_m. \qquad \text{(C5)}$$

In Eq. (C5), $\vec{v}_m, \vec{v}_n, \hat{u}_m,$ and $\hat{u}_n$ are defined as

$$\vec{v}_m = (m \cos a, m \sin a), \qquad \text{(C6)}$$

$$\vec{v}_n = (n \cos b, n \sin b), \qquad \text{(C7)}$$

$$\hat{u}_m = (\cos d, \sin d), \qquad \text{(C8)}$$

and

$$\hat{u}_n = (\cos e, \sin e), \qquad \text{(C9)}$$

where m and n are the magnitudes of $\vec{v}_m$ and $\vec{v}_n$, respectively, and the angles $a, b, d,$ and e are the orientations of $\vec{v}_m, \vec{v}_n, \hat{u}_m,$ and $\hat{u}_n$, respectively. The contact distance r_{ji} is

$$r_{ji} = |q \cos(d + \theta_i) - m \sin(a - d) + n \sin \beta$$
$$+ l_n \sin \Delta - p \sin(d + \theta_i)|, \qquad \text{(C10)}$$

where

$$\beta = b - d + \theta_j - \theta_i \qquad \text{(C11)}$$

and

$$\Delta = e - d + \theta_j - \theta_i. \qquad \text{(C12)}$$

The nonzero first and second derivatives can be expressed as

$$\frac{\partial r_{ji}}{\partial x_i} = \Xi \sin(d + \theta_i), \qquad \text{(C13)}$$

$$\frac{\partial r_{ji}}{\partial y_i} = -\Xi \cos(d + \theta_i), \qquad \text{(C14)}$$

$$\frac{\partial r_{ji}}{\partial \theta_i} = -\Xi [n \cos \beta + l_n \cos \Delta$$
$$+ p \cos(d + \theta_i) + q \sin(d + \theta_i)], \qquad \text{(C15)}$$

$$\frac{\partial r_{ji}}{\partial x_j} = -\frac{\partial r_{ji}}{\partial x_i}, \qquad \text{(C16)}$$

$$\frac{\partial r_{ji}}{\partial y_j} = -\frac{\partial r_{ji}}{\partial y_i}, \qquad \text{(C17)}$$

$$\frac{\partial r_{ji}}{\partial \theta_j} = -\Xi [n \cos \beta + l_n \cos \Delta], \qquad \text{(C18)}$$

$$\frac{\partial^2 r_{ji}}{\partial x_i \partial \theta_i} = -\frac{\partial r_{ji}}{\partial y_i}, \qquad \text{(C19)}$$

$$\frac{\partial^2 r_{ji}}{\partial y_i \partial \theta_i} = \frac{\partial r_{ji}}{\partial x_i}, \qquad \text{(C20)}$$

$$\frac{\partial^2 r_{ji}}{\partial \theta_i \partial \theta_i} = -\Xi [n \sin \beta + l_n \sin \Delta$$
$$- p \sin(d + \theta_i) + q \cos(d + \theta_i)], \qquad \text{(C21)}$$

$$\frac{\partial^2 r_{ji}}{\partial x_j \partial \theta_i} = \frac{\partial r_{ji}}{\partial y_i}, \qquad \text{(C22)}$$

$$\frac{\partial^2 r_{ji}}{\partial y_j \partial \theta_i} = -\frac{\partial r_{ji}}{\partial x_i}, \qquad \text{(C23)}$$

$$\frac{\partial^2 r_{ji}}{\partial \theta_j \partial \theta_i} = \Xi [n \sin \beta + l_n \sin \Delta], \qquad \text{(C24)}$$

and

$$\frac{\partial^2 r_{ji}}{\partial \theta_j \partial \theta_j} = -\frac{\partial^2 r_{ji}}{\partial \theta_j \partial \theta_i}. \qquad \text{(C25)}$$

In the expressions in Eqs. (C13)–(C25), Ξ is defined as

$$\Xi = \text{Sgn}[q \cos(d + \theta_i) - m \sin(a - d) + n \sin \beta$$
$$+ l_n \sin \Delta - p \sin(d + \theta_i)], \qquad \text{(C26)}$$

where

$$\text{Sgn}(z) = \begin{cases} 1, & z > 0 \\ 0, & z = 0 \\ -1, & z < 0. \end{cases} \qquad \text{(C27)}$$

All of the other first and second derivatives are zero.

The second type of contact between circulo-polygons is a contact between two vertices. In this case, l_m and l_n are each half the lengths of edges m and n, respectively. The x and y components of separation vector $\vec{r}_{ji}$ are

$$x_{ji} = p + n \cos(b + \theta_j) + l_n \cos(e + \theta_j)$$
$$- m \cos(a + \theta_i) - l_m \cos(d + \theta_i) \qquad \text{(C28)}$$

and

$$y_{ji} = q + n\sin(b+\theta_j) + l_n\sin(e+\theta_j)$$
$$- m\sin(a+\theta_i) - l_m\sin(d+\theta_i). \quad \text{(C29)}$$

For vertex-vertex contacts, the nonzero first and second derivatives are

$$\frac{\partial r_{ji}}{\partial x_i} = -\frac{x_{ji}}{r_{ji}}, \quad \text{(C30)}$$

$$\frac{\partial r_{ji}}{\partial y_i} = -\frac{y_{ji}}{r_{ji}}, \quad \text{(C31)}$$

$$\frac{\partial r_{ji}}{\partial \theta_i} = \frac{1}{r_{ji}}\{-l_m[q\cos(d+\theta_i) - p\sin(d+\theta_i)$$
$$+ n\sin\beta + l_n\sin\Delta] + m[p\sin(a+\theta_i)$$
$$- q\cos(a+\theta_i) - n\sin\omega + l_n\sin\mu]\}, \quad \text{(C32)}$$

$$\frac{\partial r_{ji}}{\partial x_j} = -\frac{\partial r_{ji}}{\partial x_i}, \quad \text{(C33)}$$

$$\frac{\partial r_{ji}}{\partial y_j} = -\frac{\partial r_{ji}}{\partial y_i}, \quad \text{(C34)}$$

$$\frac{\partial r_{ji}}{\partial \theta_j} = \frac{1}{r_{ji}}\{l_n[q\cos(e+\theta_j) - p\sin(e+\theta_j)$$
$$- m\sin\mu + l_m\sin\Delta] + n[q\cos(b+\theta_j)$$
$$- p\sin(b+\theta_j) + m\sin\omega + l_m\sin\beta]\}, \quad \text{(C35)}$$

$$\frac{\partial \vec{r}_{ji}}{\partial x_i} \cdot \frac{\partial \vec{r}_{ji}}{\partial x_i} = \frac{\partial \vec{r}_{ji}}{\partial y_i} \cdot \frac{\partial \vec{r}_{ji}}{\partial y_i} = \frac{\partial \vec{r}_{ji}}{\partial x_j} \cdot \frac{\partial \vec{r}_{ji}}{\partial x_j} = \frac{\partial \vec{r}_{ji}}{\partial y_j} \cdot \frac{\partial \vec{r}_{ji}}{\partial y_j} = 1, \quad \text{(C36)}$$

$$\frac{\partial \vec{r}_{ji}}{\partial x_i} \cdot \frac{\partial \vec{r}_{ji}}{\partial x_j} = \frac{\partial \vec{r}_{ji}}{\partial y_i} \cdot \frac{\partial \vec{r}_{ji}}{\partial y_j} = -1, \quad \text{(C37)}$$

$$\frac{\partial \vec{r}_{ji}}{\partial x_i} \cdot \frac{\partial \vec{r}_{ji}}{\partial \theta_i} = -m\sin(a+\theta_i) - l_m\sin(d+\theta_i), \quad \text{(C38)}$$

$$\frac{\partial \vec{r}_{ji}}{\partial x_i} \cdot \frac{\partial \vec{r}_{ji}}{\partial \theta_j} = n\sin(b+\theta_i) + l_n\sin(e+\theta_j), \quad \text{(C39)}$$

$$\frac{\partial \vec{r}_{ji}}{\partial y_i} \cdot \frac{\partial \vec{r}_{ji}}{\partial \theta_i} = m\cos(a+\theta_i) + l_m\cos(d+\theta_i), \quad \text{(C40)}$$

$$\frac{\partial \vec{r}_{ji}}{\partial y_i} \cdot \frac{\partial \vec{r}_{ji}}{\partial \theta_j} = -n\cos(b+\theta_i) - l_n\cos(e+\theta_j), \quad \text{(C41)}$$

$$\frac{\partial \vec{r}_{ji}}{\partial \theta_i} \cdot \frac{\partial \vec{r}_{ji}}{\partial \theta_i} = l_m^2 + m^2 + 2l_m m\cos(a-d), \quad \text{(C42)}$$

$$\frac{\partial \vec{r}_{ji}}{\partial \theta_i} \cdot \frac{\partial \vec{r}_{ji}}{\partial x_j} = -\frac{\partial \vec{r}_{ji}}{\partial x_i} \cdot \frac{\partial \vec{r}_{ji}}{\partial \theta_i}, \quad \text{(C43)}$$

$$\frac{\partial \vec{r}_{ji}}{\partial \theta_i} \cdot \frac{\partial \vec{r}_{ji}}{\partial y_j} = -\frac{\partial \vec{r}_{ji}}{\partial y_i} \cdot \frac{\partial \vec{r}_{ji}}{\partial \theta_i}, \quad \text{(C44)}$$

$$\frac{\partial \vec{r}_{ji}}{\partial \theta_i} \cdot \frac{\partial \vec{r}_{ji}}{\partial \theta_j} = -n(l_m\cos\beta + m\cos\omega)$$
$$- l_n(l_m\cos\Delta + m\cos\mu), \quad \text{(C45)}$$

$$\frac{\partial \vec{r}_{ji}}{\partial x_j} \cdot \frac{\partial \vec{r}_{ji}}{\partial \theta_j} = -\frac{\partial \vec{r}_{ji}}{\partial x_i} \cdot \frac{\partial \vec{r}_{ji}}{\partial \theta_j}, \quad \text{(C46)}$$

$$\frac{\partial \vec{r}_{ji}}{\partial y_j} \cdot \frac{\partial \vec{r}_{ji}}{\partial \theta_j} = -\frac{\partial \vec{r}_{ji}}{\partial y_i} \cdot \frac{\partial \vec{r}_{ji}}{\partial \theta_j}, \quad \text{(C47)}$$

$$\frac{\partial \vec{r}_{ji}}{\partial \theta_j} \cdot \frac{\partial \vec{r}_{ji}}{\partial \theta_j} = l_n^2 + n^2 + 2l_n n\cos(b-e), \quad \text{(C48)}$$

and

$$\vec{r}_{ji} \cdot \frac{\partial^2 \vec{r}_{ji}}{\partial \theta_i \partial \theta_i} = -\frac{\partial \vec{r}_{ji}}{\partial \theta_i} \cdot \frac{\partial \vec{r}_{ji}}{\partial \theta_i} - \frac{\partial \vec{r}_{ji}}{\partial \theta_i} \cdot \frac{\partial \vec{r}_{ji}}{\partial \theta_j}$$
$$+ p\frac{\partial \vec{r}_{ji}}{\partial y_i} \cdot \frac{\partial \vec{r}_{ji}}{\partial \theta_i} - q\frac{\partial \vec{r}_{ji}}{\partial x_i} \cdot \frac{\partial \vec{r}_{ji}}{\partial \theta_i}, \quad \text{(C49)}$$

$$\vec{r}_{ji} \cdot \frac{\partial^2 \vec{r}_{ji}}{\partial \theta_j \partial \theta_j} = -\frac{\partial \vec{r}_{ji}}{\partial \theta_j} \cdot \frac{\partial \vec{r}_{ji}}{\partial \theta_j} - \frac{\partial \vec{r}_{ji}}{\partial \theta_i} \cdot \frac{\partial \vec{r}_{ji}}{\partial \theta_j}$$
$$+ p\frac{\partial \vec{r}_{ji}}{\partial y_i} \cdot \frac{\partial \vec{r}_{ji}}{\partial \theta_j} - q\frac{\partial \vec{r}_{ji}}{\partial x_i} \cdot \frac{\partial \vec{r}_{ji}}{\partial \theta_j}, \quad \text{(C50)}$$

where

$$\omega = b - a + \theta_j - \theta_i \quad \text{(C51)}$$

and

$$\mu = a - e - \theta_j + \theta_i. \quad \text{(C52)}$$

The other derivatives $\frac{\partial \vec{r}_{ji}}{\partial \xi_i} \cdot \frac{\partial \vec{r}_{ji}}{\partial \xi_j}$ and $\vec{r}_{ji} \cdot \frac{\partial^2 \vec{r}_{ji}}{\partial \xi_i \partial \xi_j}$ that are not listed above are zero.

[1] C. S. O'Hern, L. E. Silbert, A. J. Liu, and S. R. Nagel, Phys. Rev. E **68**, 011306 (2003).

[2] A. J. Liu and S. R. Nagel, Annu. Rev. Condens. Matter Phys. **1**, 347 (2010).

[3] M. van Hecke, J. Phys.: Condens. Matter **22**, 033101 (2009).

[4] A. Donev, R. Connelly, F. H. Stillinger, and S. Torquato, Phys. Rev. E **75**, 051304 (2007).

[5] M. Mailman, C. F. Schreck, C. S. O'Hern, and B. Chakraborty, Phys. Rev. Lett. **102**, 255501 (2009).

[6] C. F. Schreck, M. Mailman, B. Chakraborty, and C. S. O'Hern, Phys. Rev. E **85**, 061305 (2012).

[7] Z. Zeravcic, N. Xu, A. J. Liu, S. R. Nagel, and W. van Saarloos, Europhys. Lett. **87**, 26001 (2009).

[8] M. G. Basavaraj, G. G. Fuller, J. Fransaer, and J. Vermant, Langmuir **22**, 6605 (2006).

[9] F. M. Schaller, M. Neudecker, M. Saadatfar, G. W. Delaney, G. E. Schröder-Turk, and M. Schröter, Phys. Rev. Lett. **114**, 158001 (2015).

[10] A. Donev, I. Cisse, D. Sachs, E. A. Variano, F. H. Stillinger, R. Connelly, S. Torquato, and P. M. Chaikin, Science **303**, 990 (2004).

[11] W. Man, A. Donev, F. H. Stillinger, M. T. Sullivan, W. B. Russel, D. Heeger, S. Inati, S. Torquato, and P. M. Chaikin, Phys. Rev. Lett. **94**, 198001 (2005).

[12] J. Zhao, S. Li, R. Zou, and A. Yu, Soft Matter **8**, 1003 (2012).

[13] J. Blouwolff and S. Fraden, Europhys. Lett. **76**, 1095 (2006).

[14] S. R. Williams and A. P. Philipse, Phys. Rev. E **67**, 051301 (2003).

[15] L. Meng, Y. Jiao, and S. Li, Powder Technol. **292**, 176 (2016).

[16] A. Wouterse, S. R. Williams, and A. P. Philipse, J. Phys.: Condens. Matter **19**, 406215 (2007).

[17] A. Wouterse, S. Luding, and A. P. Philipse, Granular Matter **11**, 169 (2009).

[18] Y. Jiao and S. Torquato, Phys. Rev. E **84**, 041309 (2011).

[19] E. R. Chen, D. Klotsa, M. Engel, P. F. Damasceno, and S. C. Glotzer, Phys. Rev. X **4**, 011024 (2014).

[20] C. F. Schreck, N. Xu, and C. S. O'Hern, Soft Matter **6**, 2960 (2010).

[21] J. C. Gaines, A. H. Clark, L. Regan, and C. S. O'Hern, J. Phys.: Condens. Matter **29**, 293001 (2017).

[22] M. Z. Miskin and H. M. Jaeger, Nat. Mater. **12**, 326 (2013).

[23] A. Baule, R. Mari, L. Bo, L. Portal, and H. A. Makse, Nat. Commun. **4**, 2194 (2013).

[24] A. V. Tkachenko and T. A. Witten, Phys. Rev. E **60**, 687 (1999).

[25] S. Papanikolaou, C. S. O'Hern, and M. D. Shattuck, Phys. Rev. Lett. **110**, 198002 (2013).

[26] C. Wang, K. Dong, and A. Yu, Phys. Rev. E **92**, 062203 (2015).

[27] Y. Han and M. W. Kim, Soft Matter **8**, 9015 (2012).

[28] S. Atkinson, Y. Jiao, and S. Torquato, Phys. Rev. E **86**, 031302 (2012).

[29] S. M. Rubio-Largo, F. Alonso-Marroquin, T. Weinhart, S. Luding, and R. C. Hidalgo, Phys. A (Amsterdam) **443**, 477 (2016).

[30] F. Alonso-Marroquin and Y. Wang, Granular Matter **11**, 317 (2009).

[31] F. Alonso-Marroquin, Europhys. Lett. **83**, 14001 (2008).

[32] S. A. Galindo-Torres, J. D. Muñoz, and F. Alonso-Marroquin, Phys. Rev. E **82**, 056713 (2010).

[33] M. Spellings, R. L. Marson, J. A. Anderson, and S. C. Glotzer, J. Comput. Phys. **334**, 460 (2017).

[34] R. J. Speedy, J. Phys.: Condens. Matter **10**, 4185 (1998).

[35] N. Xu, J. Blawzdziewicz, and C. S. O'Hern, Phys. Rev. E **71**, 061306 (2005).

[36] K. C. Smith, I. Srivastava, T. S. Fisher, and M. Alam, Phys. Rev. E **89**, 042203 (2014).

[37] A. Tanguy, J. P. Wittmer, F. Leonforte, and J.-L. Barrat, Phys. Rev. B **66**, 174205 (2002).

[38] J. Tian, Y. Xu, Y. Jiao, and S. Torquato, Sci. Rep. **5**, 16722 (2015).

[39] T. Marschall and S. Teitel, Phys. Rev. E **97**, 012905 (2018).

[40] J. N. Roux, Phys. Rev. E **61**, 6802 (2000).

[41] P. F. Damasceno, M. Engel, and S. C. Glotzer, Science **337**, 453 (2012).

[42] P. F. Damasceno, M. Engel, and S. C. Glotzer, ACS Nano **6**, 609 (2012).

[43] M. E. Irrgang, M. Engel, A. J. Schultz, D. A. Kofke, and S. C. Glotzer, Langmuir **33**, 11788 (2017).

[44] G. E. Schröder-Turk, W. Mickel, S. C. Kapfer, F. M. Shaller, B. Breidenbach, D. Hug, and K. Mecke, New J. Phys. **15**, 083028 (2013).

[45] C. F. Schreck, C. S. O'Hern, and M. D. Shattuck, Granular Matter **16**, 209 (2014).

[46] E. Oks and M. Sharir, Discrete Comput. Geom. **35**, 223 (2006).